AIAA JOURNAL
Vol. 36, No. 2, February 1998

Electrode Pattern Design of Piezoelectric Sensors and Actuators Using Genetic Algorithms

Jung-Kyu Ryou,* Keun-Young Park,† and Seung-Jo Kim‡
Seoul National University, Seoul 151-742, Republic of Korea

A distributed piezoelectric sensor and actuator have been designed for the efficient vibration control of a plate. Optimization of the electrode pattern of polyvinylidene fluoride (PVDF) film has been performed to realize the concept of modal transducer for a two-dimensional structure. The finite element method is used to model the structure that includes the PVDF sensor and actuator. Various lamination angles of transducers are taken into consideration to utilize the anisotropy of the PVDF film. The electrode pattern over the entire surface of the plate is determined by deciding on or off of each electrode segment. The actuator design is based on the criterion of minimizing the system energy in the control modes under a given initial condition. The sensor is designed to minimize the observation spillover. Modal control forces for the residual (uncontrolled) modes have been minimized during the sensor design. A genetic algorithm, which is suitable for this kind of discrete problem, has been utilized for optimization. A discrete linear quadratic Gaussian control law has been applied to the integrated structure for real-time vibration control. The performance of the sensor, the actuator, and the integrated smart structure has been demonstrated by experiments.

Introduction

PIEZOELECTRIC materials are being widely used as sensors and actuators in the active vibration control of structures. Lead zirconate titanate (PZT) and polyvinylidene fluoride (PVDF) are the most popular ones. Because of the large actuation force of PZT, there has been much research on the use of PZT as a sensor and an actuator. Concern is given to the positioning and the sizing of PZT. PVDF has an advantage in the relative easiness of electrode pattern shading, in addition to its flexibility and light weight. Research related to PVDF has focused on the electrode pattern of the PVDF transducer. Selection of an electrode pattern in a one-dimensional application is relatively easy. We can regulate the modal force of each mode by changing the width of the electrode.[1] Since the concept of the spatial filter was introduced by Bailey and Hubbard,[2] it has been extended to two-dimensional structures by Hubbard and Burke.[3] Lee and Moon[4] have shown the performance of modal sensors and actuators. The effect of the shaped piezoceramic on the excitation force[5] is similar to that of the electrode shaping of the PVDF transducer. It is, however, hard to apply the concept of a modal transducer in vibration control of two-dimensional structures. Burke and Sullivan[6] presented the concepts of a spatial gradient electrode and optimized electrode shapes for a plate.

In this study, we introduce an electrode lattice over the entire surface of a plate and optimize the electrode pattern and the lamination angle of the PVDF transducer. We can adjust modal actuation forces by determining on or off of each electrode segment. The electrode in the segment selected to be off will be removed by chemical etching. The PVDF film in this segment, therefore, does not contribute to actuation or sensing.

The real-time vibration control of a plate will be given in this study. A discrete linear quadratic Gaussian (LQG) control law is used for vibration control. Because the size of the system model for building the state estimator is limited, modal reduction is prerequisite. This reduction may cause a spillover[7] phenomenon that may degrade the stability in residual modes. As pointed out by Lee,[1] the modal sensor does work to prevent the adverse effect of spillover. This study presents a methodology to design a two-dimensional PVDF transducer that acts as a distributed spatial filter for the efficient vibration control of a plate. A genetic algorithm is utilized to optimize the electrode pattern of the PVDF transducer. Experiments have been conducted to observe the performance of the designed PVDF sensor, actuator, and integrated smart structure.

System Model

Effect of Electrode Shape

Reciprocity exists between a piezoelectric sensor and actuator. A piezoelectric sensor that yields a large amount of charge for a specific vibration mode will have a large actuating force for the mode when used as an actuator. The sensor equation[1] says that the amount of induced charge q in a piezoelectric sensor is

$$
\begin{aligned}
q &= -z \int_s \left[\bar{e}_{31(xy)} \frac{\partial^2 w}{\partial x^2} + \bar{e}_{32(xy)} \frac{\partial^2 w}{\partial y^2} + 2\bar{e}_{36(xy)} \frac{\partial^2 w}{\partial x \partial y} \right] \mathrm{d}S \\
&= \int_s \left[\bar{e}_{31(xy)} \varepsilon_x + \bar{e}_{32(xy)} \varepsilon_y + \bar{e}_{36(xy)} \gamma_{xy} \right] \mathrm{d}S
\end{aligned} \tag{1}
$$

where z is the distance from the neutral plane to the midplane of the sensor, w is the lateral displacement, S is the effective area of sensor covered with the electrode, and $\bar{e}$ and ε are piezoelectric constants and strain components, respectively. From Eq. (1), we can see that the amount of induced charge will increase if the piezoelectric sensor is located in a highly strained region. Let us consider the case where the sign of strain changes from point to point in the region covered by the piezoelectric sensor. The charge induced in the positively strained area is canceled out by the charge induced in the negatively strained area, which leads to a decrease of the total charge. The piezoelectric constants $\bar{e}_{ij(xy)}$ vary with the lamination angle of the anisotropic PVDF film. Therefore, both the electrode pattern and the lamination angle of a PVDF transducer become important. For the same reason,[8] the size and position of the PZT transducer have been given attention.

Structural Model

The finite element method is used to model the plate integrated with the piezoelectric sensor and actuator. Nine-node Reissner–Mindlin plate elements are used. Each node has five degrees of freedom (Fig. 1), three in displacement and two in rotation.

Received Feb. 28, 1997; presented as Paper 97-1348 at the AIAA/ASME/AHS Adaptive Structures Forum, Kissimmee, FL, April 7–10, 1997; revision received Aug. 10, 1997; accepted for publication Sept. 26, 1997.

*Research Assistant, Department of Aerospace Engineering; currently Senior Researcher, Airframe Structures Division, 3rd R&D Center, Agency for Defense Development, Daejeon 305-600, Republic of Korea.

†Research Assistant, Department of Aerospace Engineering; currently Engineer, Passenger Car Chassis and Powertrain Engineering Team #1, Hyundai Motor Company, Ulsan 681-791, Republic of Korea.

‡Professor, Department of Aerospace Engineering. Member AIAA.

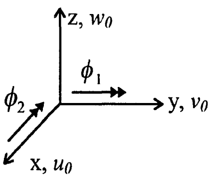

Fig. 1 Degrees of freedom at each node in finite elements.

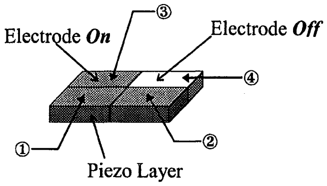

Fig. 2 Plate element with four electrode segments.

The piezoelectric sensor and the actuator are divided into rectangular segments to describe the pattern over the entire surface of the plate. The cantilevered plate in the present study is modeled with 24 finite elements. We have divided each finite element into four electrode segments (Fig. 2) to represent the piezoelectric force. The total number of electrode segments is 4 × 24 = 96 each for the sensor and the actuator.

The actuating force of the ith piezoelectric segment per unit voltage, $\boldsymbol{F}_p^{(i)}$, is as follows:

$$\boldsymbol{F}_p^{(i)} = \int_{V^{(i)}} \frac{\boldsymbol{B}_I^{(i)T} \hat{\boldsymbol{e}}^{(i)}\, \mathrm{d}V^{(i)}}{t^{(i)}} \tag{2}$$

where $\boldsymbol{B}_I^{(i)}$ is the interpolation matrix of the in-plane strain, $\hat{\boldsymbol{e}}^{(i)}$ is the piezoelectric matrix, and $t^{(i)}$ is the thickness of the piezoelectric segment.

The element force of a piezoelectric actuator $\boldsymbol{B}_a^e$, composed of many piezoelectric segments, is

$$\boldsymbol{B}_a^e = \sum_i S(i)\boldsymbol{F}_p^{(i)} \tag{3}$$

where $S(i) = 1$ if the electrode segment is on and $S(i) = 0$ if the electrode segment is off. The $\boldsymbol{S}$ vector in Eq. (3) determines the electrode pattern. This is the design variable in this study. Electrode segments are determined to be on or off during the optimization process of the sensor and the actuator. The electrode on the segment selected to be off will be removed, and thus, this segment has no actuating force. All of the electrode segments selected to be on are electrically connected. For example, let us consider four electrode segments in a plate element, as in Fig. 2. If the electrode segments 1, 2, and 3 are selected to be on and segment 4 is selected to be off, then the total actuation force by the piezoelectric actuator in the plate element is as follows:

$$\boldsymbol{B}_a^e = 1 \times \left[\boldsymbol{F}_p^{(1)} + \boldsymbol{F}_p^{(2)} + \boldsymbol{F}_p^{(3)}\right] + 0 \times \boldsymbol{F}_p^{(4)} \tag{4}$$

The equation of motion of the integrated structure is

$$\boldsymbol{M}\ddot{\boldsymbol{u}} + \boldsymbol{K}\boldsymbol{u} = \boldsymbol{B}_a V_a \tag{5}$$

where $\boldsymbol{M}$, $\boldsymbol{K}$, and $\boldsymbol{B}_a$ are the mass and the stiffness matrices and the force vector, respectively, and $\boldsymbol{u}$ is the discretized nodal displacement vector. Subscript a is the actuator, and V_a is voltage applied to the actuator. According to the reciprocity,[1] if the actuation force by a piezoelectric transducer is $\boldsymbol{B}_s$, then the electric charge induced in this transducer when used as a sensor is

$$q = \boldsymbol{B}_s^T \boldsymbol{u} \tag{6}$$

where subscript s is the sensor. This equation is the same as the discretized form of Eq. (1). Modal reduction is used for computational efficiency. Let $\boldsymbol{\Phi}_R$ and $\boldsymbol{\Lambda}_R$ be the matrices composed of the eigenvectors and the eigenvalues of Eq. (5), i.e., $\Lambda_i \boldsymbol{M}\boldsymbol{\phi}_i = \boldsymbol{K}\boldsymbol{\phi}_i$, and so

$$\boldsymbol{\Phi}_R = [\boldsymbol{\phi}_1 \quad \cdots \quad \boldsymbol{\phi}_n] \tag{7}$$

$$\boldsymbol{\Lambda}_R = \mathrm{diag}(\Lambda_1 \quad \cdots \quad \Lambda_n) \tag{8}$$

Eigenvectors are normalized as follows:

$$\boldsymbol{\Phi}_R^T \boldsymbol{M} \boldsymbol{\Phi}_R = \boldsymbol{I}, \qquad \boldsymbol{\Phi}_R^T \boldsymbol{K} \boldsymbol{\Phi}_R = \boldsymbol{\Lambda}_R \tag{9}$$

Assuming modal viscous damping, Eq. (5) is expressed in modal coordinates:

$$\ddot{\boldsymbol{\eta}}_R + \boldsymbol{c}_R \dot{\boldsymbol{\eta}}_R + \boldsymbol{\Lambda}_R \boldsymbol{\eta}_R = \boldsymbol{\Phi}_R^T \boldsymbol{B}_a V_a \tag{10}$$

where $\boldsymbol{c}_R = \mathrm{diag}(2\zeta_1\omega_1 \ldots 2\zeta_n\omega_n)$, $\omega_i^2 = \Lambda_i$, and $\boldsymbol{\eta}_R$ is modal displacement. Damping coefficients ζ_i are assumed to be 0.001. From Eq. (10), we define $\boldsymbol{\Phi}_R^T \boldsymbol{B}_a$ as modal control force per unit voltage, and it is used as a parameter for characterizing the modal performance of the piezoelectric sensors and actuators.

Total System and Control Environment

We need to combine the design of sensors and actuators with a specific control law. The LQG method was used as a control law. Figure 3 shows the block diagram of the total system. Because we use a digital controller with an antialiasing low-pass filter, there exists a finite controller bandwidth. It primarily depends on the sampling frequency and the cutoff frequency of the filter. Every mode in this controller bandwidth needs to be included in the closed-loop simulation. Because a charge amplifier is used as an interfacing circuit, the sensor output through the amplifier is

$$y_{ca} = (1/C_a)\boldsymbol{B}_s^T \boldsymbol{\Phi}_R \boldsymbol{\eta}_R \tag{11}$$

where $1/C_a$ is the gain of the charge amplifier.

Two low-pass filters are used before the A/D converter and after the D/A converter to prevent the aliasing and the high-frequency noise due to the zero-order hold, respectively. The state-space form of the total system is as follows:

$$\dot{z} = \begin{bmatrix} \dot{\boldsymbol{\eta}}_R \\ \ddot{\boldsymbol{\eta}}_R \\ \dot{\boldsymbol{x}}_{fi} \\ \dot{\boldsymbol{x}}_{fo} \end{bmatrix} = \begin{bmatrix} \boldsymbol{0} & \boldsymbol{I} & \boldsymbol{0} & \boldsymbol{0} \\ -\boldsymbol{\Lambda}_R & \boldsymbol{c}_R & \boldsymbol{0} & K_{\mathrm{amp}}\boldsymbol{\Phi}_R^T\boldsymbol{B}_a\boldsymbol{C}_f \\ (1/C_a)\boldsymbol{B}_f\boldsymbol{B}_s^T\boldsymbol{\Phi}_R & \boldsymbol{0} & \boldsymbol{A}_f & \boldsymbol{0} \\ \boldsymbol{0} & \boldsymbol{0} & \boldsymbol{0} & \boldsymbol{A}_f \end{bmatrix} z + \begin{bmatrix} \boldsymbol{0} \\ \boldsymbol{0} \\ \boldsymbol{0} \\ \boldsymbol{B}_f \end{bmatrix} V_a \tag{12a}$$

$$y = \begin{bmatrix} \boldsymbol{0} & \boldsymbol{0} & \boldsymbol{C}_f & \boldsymbol{0} \end{bmatrix} z \tag{12b}$$

In Eq. (12), $\boldsymbol{x}_{fi}$ and $\boldsymbol{x}_{fo}$ are the states of the low-pass filter at the input and the output of the controller, respectively; $\boldsymbol{A}_f$, $\boldsymbol{B}_f$, and $\boldsymbol{C}_f$ are the state matrices of the low-pass filter; and K_{amp} is the gain of the high-voltage amplifier involved.

For real-time control, it is necessary to limit the size of the controller. Therefore, we have divided the mode vector $\boldsymbol{\eta}_R$ into the modes to be controlled $\boldsymbol{\eta}_c$ and the modes to be uncontrolled $\boldsymbol{\eta}_u$:

$$\boldsymbol{\eta}_R = \begin{bmatrix} \boldsymbol{\eta}_c \\ \boldsymbol{\eta}_u \end{bmatrix} \tag{13}$$

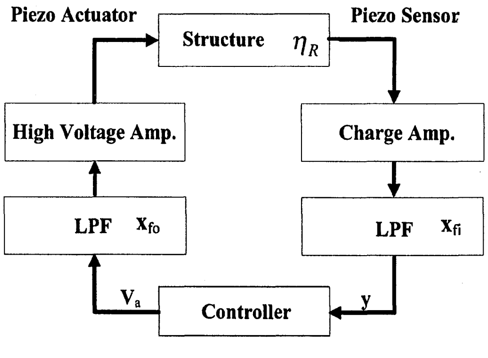

Fig. 3 Block diagram for the total system.

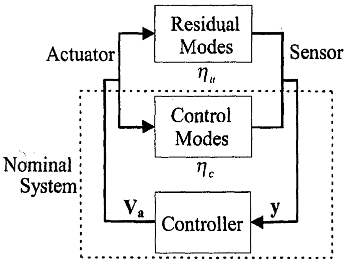

Fig. 4 Schematic diagram of the spillover.

and total system state z is divided into z_c and z_u. Equation (12) can be rewritten as follows:

$$\dot{z}_c = \begin{bmatrix} \dot{\eta}_c \\ \ddot{\eta}_c \\ \dot{x}_{fi} \\ \dot{x}_{fo} \end{bmatrix} = \boldsymbol{A}_c z_c + \boldsymbol{B}_c V_a \tag{14a}$$

$$\dot{z}_u = \begin{bmatrix} \dot{\eta}_u \\ \ddot{\eta}_u \end{bmatrix} = \boldsymbol{A}_u z_u + \boldsymbol{B}_u V_a \tag{14b}$$

$$y = \boldsymbol{C}_c z_c + \boldsymbol{C}_u z_u \tag{14c}$$

Subscripts c and u are the controlled mode and the uncontrolled mode, respectively. The nominal plant, consisting of the control modes and the filters, is discretized for controller design:

$$z_c(k+1) = \boldsymbol{\Phi}_c(T_s) z_c(k) + \Gamma_c V_a(k) \tag{15a}$$

$$y(k) = \boldsymbol{C}_c z_c(k) \tag{15b}$$

where $\boldsymbol{\Phi}_c(T_s)$ is the discretized state transition matrix of the nominal plant and T_s is the sampling time. The discrete LQG control law has the following forms:

$$\bar{z}_c(k+1) = [\boldsymbol{\Phi}_c(T_s) - \boldsymbol{\Phi}_c(T_s)\boldsymbol{K}_f\boldsymbol{C}_c - \Gamma_c\boldsymbol{K}_c]\bar{z}_c(k) + \boldsymbol{\Phi}_c(T_s)\boldsymbol{K}_f y(k) \tag{16a}$$

$$\boldsymbol{u}(k) = -\boldsymbol{K}_c \bar{z}_c(k) \tag{16b}$$

where $\bar{z}_c$ is the estimated nominal states, $\boldsymbol{K}_f$ is the Kalman filter gain, and $\boldsymbol{K}_c$ is the control gain from LQR.

Spillover and Spatial Filter

As we can control only a few modes out of the infinite number of structural modes, spillover may occur. Figure 4 shows the generation of the spillover. Spillover is composed of the observation spillover (sensing the residual modes) and the control spillover (actuating the residual modes). Control spillover acts as a low-frequency disturbance to the residual modes, whereas observation spillover as a high-frequency noise to the control modes. Residual modes can go unstable by the combination of these two spillovers. The occurrence of spillover does not always mean the degradation of stability. In the case that the effect of spillover does not exceed the open-loop damping, the system will not go unstable. The spillover, however, sets a limit to the gain of the controller. A typical example of spillover is chattering, which is a residue of small, high-frequency vibration during vibration control.

To avoid the spillover, we can include the residual mode that goes unstable in the controller. The computation speed of the hardware involved determines the number of modes that can be included in the controller. The shortcoming of this approach is that another spillover can occur after the modification of the controller. Another procedure is to use a time-domain filter. Usually control modes are lower modes. Filtering out the signal from the residual modes may reduce the observation spillover. A low-pass filter, however, cannot sufficiently eliminate the signal from the undesired higher mode that lies adjacent to the control modes.

If we can design a sensor or an actuator that does not sense or actuate the residual modes, spillover can be eliminated. A distributed sensor/actuator with which we reduce the spillover is a kind of filter in the space domain. It can be thought of as a modal bandpass filter that passes specific modes. To maximize the actuation force for the control modes, we did not try to avoid the control spillover. Therefore, to prevent instability, we should design a sensor that does not cause the observation spillover. In other words, we will maximize the passband signal while minimizing the stop-band signal.

Sensor and Actuator Design

Figure 5 shows the schematic view of the structure in this study. Electrode patterns of the piezoelectric sensor and actuator have been optimized for this structure. Several lamination angles (0, −15, −30, and −45 deg) of PVDF film have been considered. Mode shapes and the natural frequencies up to the sixth mode are shown in Fig. 6, where the thick line indicates the fixed boundary.

Genetic Algorithm

As already described, our design problem is not a continuous one but a discrete one. We determine whether an electrode segment is on or off. A genetic algorithm is suitable for this kind of problem. For better convergence speed, we use the improved genetic algorithm (IGA),[9] which is composed of the crossover, the mutation, and the stochastic remainder selection without replacement.

Sensor Design Criteria

Sensor design is based on the criteria of minimizing observation spillover from the residual modes. Modal control forces for the residual modes are minimized, whereas those for the control modes are maximized. The performance index to be maximized is

$$J_{\text{sensor}} = \min\left(\left|\boldsymbol{\Phi}_c^T \boldsymbol{B}_s\right|\right) - \max\left(\left|\boldsymbol{\Phi}_u^T \boldsymbol{B}_s\right|\right) \tag{17}$$

where $\boldsymbol{\Phi}_c^T \boldsymbol{B}_s$ and $\boldsymbol{\Phi}_u^T \boldsymbol{B}_s$ are the modal forces for the control modes and those for the residual modes, respectively.

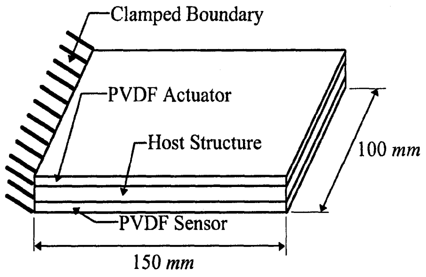

Fig. 5 Schematic view of the specimen.

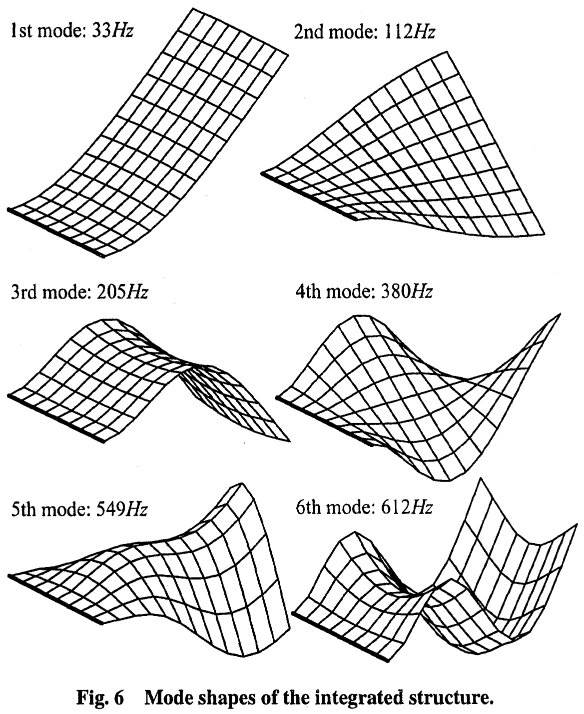

Fig. 6 Mode shapes of the integrated structure.

Actuator Design Criteria

In the course of actuator design, only the control modes are considered, as mentioned before. System energy in the control modes, E_c, is

$$E_c = \frac{1}{2}\int_0^\infty \left\{ \begin{bmatrix} \eta_c \\ \dot{\eta}_c \end{bmatrix}^T \begin{bmatrix} \Lambda_c & 0 \\ 0 & I \end{bmatrix} \begin{bmatrix} \eta_c \\ \dot{\eta}_c \end{bmatrix} \right\} \mathrm{d}t \tag{18}$$

Consider the LQR problem for the system of control modes.

Minimize:

$$J = \frac{1}{2}\int_0^\infty \left\{ \begin{bmatrix} \eta_c \\ \dot{\eta}_c \end{bmatrix}^T \boldsymbol{Q} \begin{bmatrix} \eta_c \\ \dot{\eta}_c \end{bmatrix} + V_a^T \boldsymbol{R} V_a \right\} \mathrm{d}t$$

with

$$\begin{bmatrix} \dot{\eta}_c \\ \ddot{\eta}_c \end{bmatrix} = \begin{bmatrix} \mathbf{0} & \boldsymbol{I} \\ -\Lambda_c & -\boldsymbol{C}_c \end{bmatrix} \begin{bmatrix} \eta_c \\ \dot{\eta}_c \end{bmatrix} + \begin{bmatrix} \mathbf{0} \\ \boldsymbol{\Phi}_c^T \boldsymbol{B}_a \end{bmatrix} V_a = \boldsymbol{A} \begin{bmatrix} \eta_c \\ \dot{\eta}_c \end{bmatrix} + \boldsymbol{B} V_a \tag{19}$$

Choosing $\boldsymbol{Q}$ and $\boldsymbol{R}$ as follows leads to J, the system energy in the control modes:

$$\boldsymbol{Q} = \begin{bmatrix} \Lambda_c & 0 \\ 0 & \boldsymbol{I} \end{bmatrix} \quad \text{and} \quad \boldsymbol{R} = \rho \boldsymbol{I} \tag{20}$$

The minimum of J can be obtained by solving the preceding LQR problem. $J_{\min}$ depends on the initial states:

$$J_{\min} = \frac{1}{2} \begin{bmatrix} \eta_c^0 \\ \dot{\eta}_c^0 \end{bmatrix}^T \boldsymbol{P} \begin{bmatrix} \eta_c^0 \\ \dot{\eta}_c^0 \end{bmatrix} \tag{21}$$

where $\boldsymbol{A}^T\boldsymbol{P} + \boldsymbol{P}\boldsymbol{A} + \boldsymbol{Q} - \boldsymbol{P}^T\boldsymbol{B}\boldsymbol{R}^{-1}\boldsymbol{B}^T\boldsymbol{P} = \mathbf{0}$.

The following performance index is used for actuator design:

$$J_{\text{actuator}} = \left(\sum_{k\,=\,\text{control modes}} E_0^k \right) \Bigg/ J_{\min} \tag{22}$$

where E_0^k is the initial energy in kth modes. The initial states in Eq. (21) are determined by the ratio of the initial energy in each mode. If we consider only the initial potential energy assuming zero initial kinetic energy, the following initial states can be used to evaluate the $J_{\min}$:

$$\eta_k^0 = \sqrt{E_0^k}\big/\omega_k \quad \text{and} \quad \dot{\eta}_k^0 = 0, \qquad k = 1, 2, \ldots \tag{23}$$

where ω_k is the frequency of the kth mode. We can adjust the weightings on the specific modes with the ratio of the initial energy. With the initial condition in the pure first mode, optimization yields an actuator that has maximum control force for the first mode. The weighting on the control signal, ρ in Eq. (20), has influence on the magnitude of $J_{\min}$. During the optimization of an actuator rather than a controller, however, we have found that ρ does not affect the actuator design result.

Design Result and Discussion

For the integrated structure shown in Fig. 5, the PVDF sensor and actuator have been optimized. The host structure is made of aluminum alloy, AL2024-T3, whose Young's modulus is 70 GPa, shear modulus is 26.5 GPa, and density is 2685 kg/m^3. The piezoelectric constants d_{31}, d_{32}, and d_{33} of the PVDF are 23×10^{-12}, 3×10^{-12}, and -33×10^{-12} m/V, respectively. Young's modulus of the PVDF is 3 GPa, Poisson's ratio is 0.33, and density is 1780 kg/m.

The validity of the design methodology utilized in this study is investigated first. The induced charge distribution is compared with the optimized electrode pattern. The optimized result, M4(−15 deg), is shown in Fig. 7a. It is an actuator whose actuating force in the fourth mode is maximized. The lamination angle is −15 deg. In Fig. 7b, the solid line indicates the boundary through which the sign of induced charge changes. This contour is obtained from the integrand of Eq. (1), using the deformed shape of the plate in the fourth mode. In Fig. 7, the left-hand side is the fixed edge. The active electrode in Fig. 7a coincides with the positive charge region in Fig. 7b.

Table 1 Modal force of the optimized actuator (initial condition: second mode; per unit voltage)

Mode	M2 (0 deg)	M2 (−15 deg)	M2 (−30 deg)	M2 (−45 deg)
First	1.763E−04	2.533E−04	2.349E−04	1.892E−04
Second	2.173E−04	−4.279E−04	−6.144E−04	−6.775E−04
Third	−5.477E−04	−1.044E−03	−9.886E−04	−7.306E−04
Fourth	6.724E−04	−7.535E−05	3.566E−04	5.764E−04
Fifth	5.054E−04	1.461E−03	2.034E−03	2.745E−03
Sixth	1.356E−03	1.487E−03	1.964E−03	2.341E−03
Seventh	1.316E−03	−6.511E−04	3.171E−04	7.971E−04
Eighth	−5.428E−04	−1.774E−03	−1.749E−03	−1.783E−03

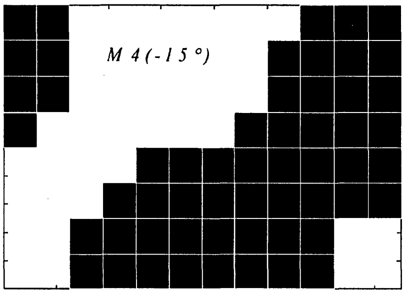

a) Optimized electrode pattern

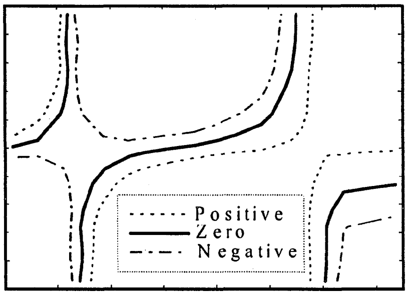

b) Distribution of the induced charge

Fig. 7 Comparison of the electrode pattern and the induced charge distribution (target mode: fourth mode and lamination angle: −15 deg).

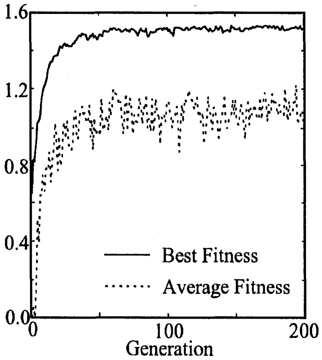

Fig. 8 Fitness curve for actuator design.

Actuator Design

For each lamination angle, an actuator has been designed with initial conditions of the first to fourth mode shapes. A total of 96 design variables are optimized using the genetic algorithm. The population in a generation is set to 100. The probabilities of crossover and mutation are 0.6 and 0.03, respectively.[9] Figure 8 shows the typical progress of the best fitness and the average fitness with generation. Improvement of the performance is obtained at the early stage.

The modal forces of the optimized PVDF actuator with the initial condition of the second mode shape are listed in Table 1. The heading M2(−30 deg) means that the target mode is the second mode and the lamination angle is −30 deg. The actuator with the lamination

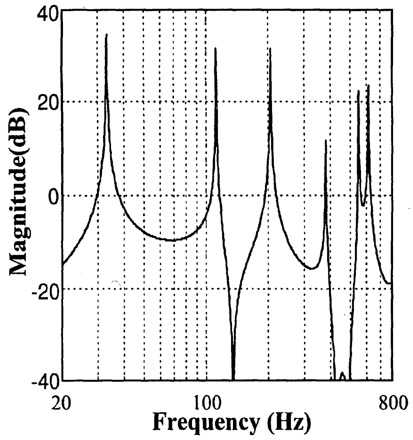

Fig. 9 Frequency response of the optimized actuator M2 (−30 deg) integrated in the structure (from numerical simulation).

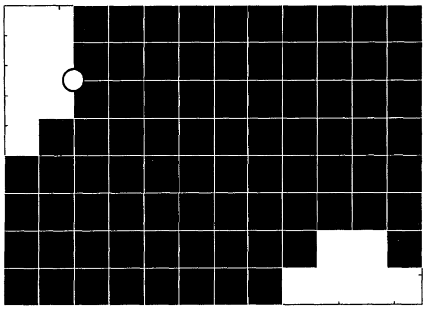

Fig. 10 Electrode pattern of the optimized actuator M2 (−30 deg) (left-hand-side edge is clamped boundary).

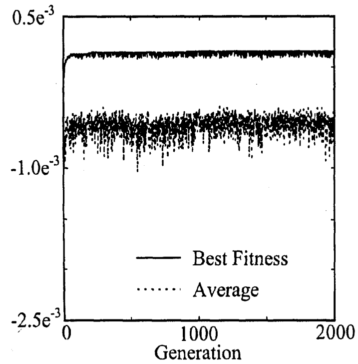

Fig. 11 Fitness curve for sensor design.

angle of −45 deg shows the largest magnitude in the second mode. Among the four actuators listed in Table 1, M2(−30 deg) is chosen for experiment. It is thought to have moderate forces in both the first and second modes. The frequency response characteristics of the actuator integrated in the structure are numerically simulated and appear in Fig. 9. The electrode pattern of M2(−30 deg) is shown in Fig. 10, where the black region is the active electrode.

Sensor Design

Design of the sensor is performed with the control modes of the first to fourth modes and the residual modes of the fifth to eighth modes. As more modes need to be considered in sensor design, a greater population in a generation is beneficial in the genetic algorithm. In this case, the population is set to 500. Figure 11 shows the typical fitness curve during optimization.

Table 2 Modal force of the optimized sensor (control mode: up to fourth mode; per unit voltage)

Mode	S4 (0 deg)	S4 (−15 deg)	S4 (−30 deg)	S4 (−45 deg)
First	1.473 E−04	1.780 E−04	1.250 E−04	1.228 E−04
Second	9.707 E−05	−1.800 E−04	−1.275 E−04	−1.333 E−04
Third	−1.090 E−04	−2.019 E−04	−1.370 E−04	1.858 E−04
Fourth	1.912 E−04	−3.383 E−04	1.443 E−04	−1.738 E−04
Fifth	1.862 E−05	1.377 E−05	−3.961 E−06	−6.554 E−06
Sixth	1.474 E−05	−4.850 E−06	3.232 E−06	1.041 E−05
Seventh	−2.147 E−06	6.596 E−06	6.105 E−07	8.617 E−06
Eighth	−2.428 E−06	−1.098 E−05	5.196 E−06	−2.046 E−06
PI	7.846 E−05	1.643 E−04	1.199 E−04	1.124 E−04

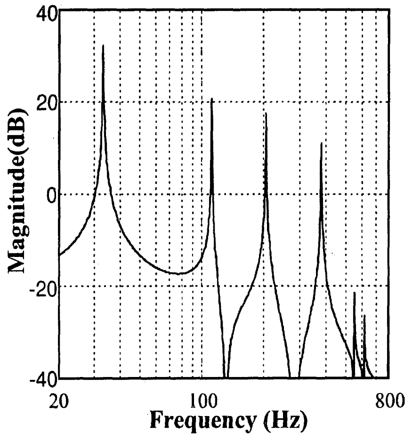

Fig. 12 Frequency response of the optimized sensor S4 (−15 deg) integrated in the structure (from numerical simulation).

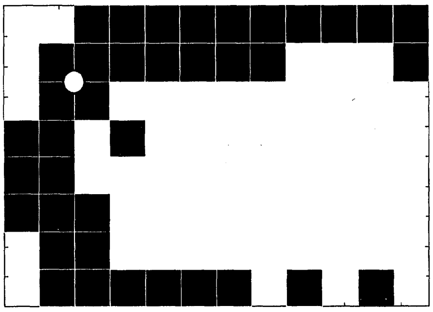

Fig. 13 Electrode pattern of the optimized sensor S4 (−15 deg) (left-hand-side edge is clamped boundary).

The modal forces and the performance indices (PI) of the optimized sensor are listed in Table 2. Heading S4 (−15 deg) indicates that four modes are included in the residual mode and the lamination angle is −15 deg. From Table 2, differences in the modal force are observed between the control modes and the residual modes. The sensor S4 (−15 deg) is selected for experiment. It shows that the magnitude of the signal from the control modes surpasses that from the residual modes by more than 20 dB. Figure 12 shows the numerical simulation of the frequency response for the sensor integrated in the structure. The amplitudes in the fifth and sixth modes show dramatic reduction compared with those of the first to fourth modes.

The electrode pattern of S4 (−15 deg) is shown in Fig. 13. Inasmuch as we have minimized the modal forces for the four residual modes in addition to maximizing those for the four control modes, it is impossible to infer a specific mode from the pattern.

Experiment

The experiment was carried out to show the performance of our integrated structure. The transfer functions of the designed PVDF sensor and actuator are obtained by the impact hammer test. During digital control using LQG, we obtain the closed-loop transfer function. Comparing it with the transfer function of the sensor, we have demonstrated the real-time vibration control.

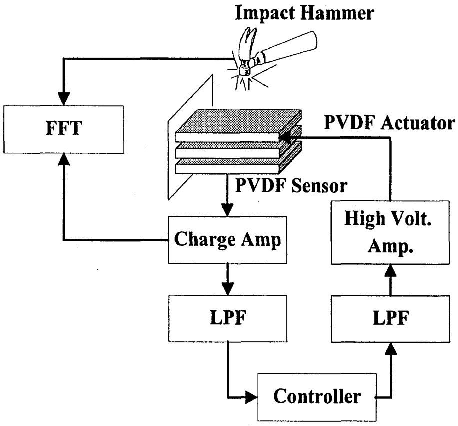

Fig. 14 Experimental setup.

Specimen Preparation

The host structure is 150 mm in length, 100 mm in width, and 1 mm in thickness and is a cantilevered plate. The thickness of the PVDF film used in this experiment is 52 μm. A photosensitizer is applied over the entire surface of PVDF film and dried in a temperature-controlled oven. After being exposed to light through the negative image of the optimized electrode pattern, the film is developed to leave a protective coating on the active electrodes. An evaporatively deposited copper–nickel electrode is chemically etched out to shape the optimized electrode pattern. Ferric chloride is used as the etchant. After washing out the etchant with water and drying, the PVDF sensor is bonded on one surface and the actuator on the other surface with epoxy adhesive. The integrated structure is completed by attaching the electric lead wire and mounts for the fixture.

Experimental Setup

Figure 14 shows the experimental setup. The charge amplifier gain is set to 10^8 V/F. Cutoff frequency of the low-pass filter is 500 Hz, which lies between the fourth and fifth frequencies of the structure. A second-order Butterworth filter is used. The sensor signal is digitally sampled 5000 times/s at the A/D converter just before the controller. The control signal from the controller is applied to the actuator through the low-pass filter and the high-voltage amplifier. Resolution of the A/D and D/A converter is 12 bit. The gain of the high-voltage amplifier is set to 100 V/V. Actual gain, therefore, equals the controller gain plus 40 dB. The total number of state variables in the controller is 12, which consists of the 8 states from the structural modes and the 4 states from the two filters involved. A matrix operation of this size is to be conducted during every sampling period. The excitation force by the impact hammer and the sensor signal from the charge amplifier are processed at the fast Fourier transform analyzer to yield the transfer function of the integrated structure. The white circle in Figs. 10 and 13 indicates the hit point during the impact hammer test. The force plus exponential data window is used.

Experimental Results and Discussion

The experimentally obtained transfer function of the sensor S4 (-15 deg) integrated in the structure is shown in Fig. 15. Comparing it with the numerical simulation in Fig. 12, we can find some discrepancy in magnitude. This is because the assumed modal viscous damping coefficients are not satisfactory. There is a need to perform further experiments to obtain more accurate damping coefficients.

The closed-loop transfer function of our integrated structure is obtained during the real-time control and is shown in Fig. 16. We can find the magnitude reduction in the control modes. The effect of control in the first and second modes is good. Because the actuator involved does not have enough actuating force for the third and fourth modes, the control effectiveness for these modes is relatively small. Figure 17 shows the time response of the closed-loop system. Settling time is reduced to $\frac{1}{5}$ compared with the open-loop system.

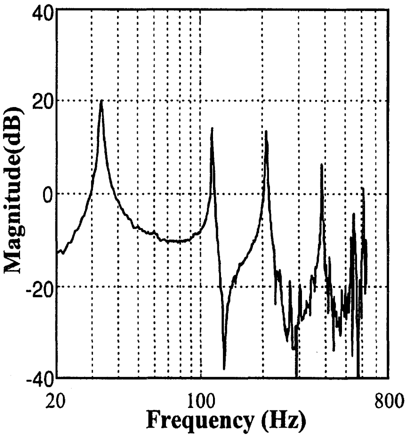

Fig. 15 Frequency response of the optimized sensor S4 (-15 deg) integrated in the structure (from experiment, open loop).

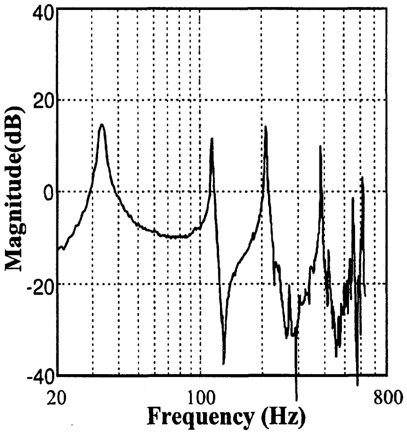

Fig. 16 Frequency response of the optimized sensor S4 (-15 deg) integrated in the structure (from experiment, closed loop).

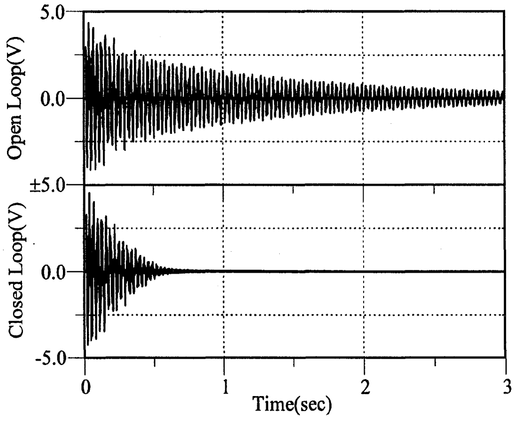

Fig. 17 Time response of the closed-loop system.

Conclusion

This research presents a new design method for a distributed sensor and actuator for the active vibration control of two-dimensional structures. The proposed method utilizes the lamination angles and electrode pattern of the PVDF film. Structural modeling using the finite element method and the genetic algorithm turned out to be useful. It led to practical realization of the modal sensor/actuator in a two-dimensional structure.

A sensor has been optimized to reduce the observation spillover, and an actuator has been optimized to maximize the modal force for a specific vibration mode. We can successfully reduce the signal from the residual modes and increase the modal force for the control mode.

Experimental verification has been accomplished to confirm the performance of the optimized sensor and actuator. Real-time vibration control has been successfully achieved for an integrated smart structure.

References

[1] Lee, C. K., "Piezoelectric Laminates: Theory for Distributed Sensors and Actuators," *Intelligent Structural Systems*, edited by H. S. Tzou and G. L. Anderson, Kluwer Academic, Norwell, MA, 1992, pp. 75–167.

[2] Bailey, T., and Hubbard, J. E., Jr., "Distributed Piezoelectric Polymer Active Vibration Control of a Cantilever Beam," *Journal of Guidance, Control, and Dynamics*, Vol. 8, No. 5, 1985, pp. 605–611.

[3] Hubbard, J. E., Jr., and Burke, S. E., "Distributed Transducer Design for Intelligent Structural Components," *Intelligent Structural Systems*, edited by H. S. Tzou, Kluwer Academic, Norwell, MA, 1992, pp. 305–324.

[4] Lee, C. K., and Moon, F. C., "Modal Sensors/Actuators," *Journal of Applied Mechanics*, Vol. 57, No. 6, 1990, pp. 434–441.

[5] Diehl, G., and Cudney, H., "The Effect of Shaped Piezoceramic Actuators on the Excitation of Beams," *Proceedings of the AIAA/ASME Adaptive Structures Forum*, AIAA, Washington, DC, 1994, pp. 270–278 (AIAA Paper 94-1763).

[6] Burke, S. E., and Sullivan, J. M., "Distributed Transducer Shading via Spatial Gradient Electrodes," *Smart Structures and Integrated Systems*, Proceedings of SPIE Smart Structures and Materials 1995, Vol. 2443, Society of Photo-Optical Instrumentation Engineers, San Diego, CA, 1995, pp. 716–726.

[7] Balas, M. J., "Feedback Control of Flexible Systems," *IEEE Transactions on Automatic Control*, Vol. AC-23, No. 4, 1978, pp. 673–679.

[8] Devasia, S., Meressi, T., Paden, B., and Bayo, E., "Piezoelectric Actuator Design for Vibration Suppression: Placement and Sizing," *Journal of Guidance, Control, and Dynamics*, Vol. 16, No. 5, 1993, pp. 859–864.

[9] Goldberg, D. E., *Genetic Algorithms in Search, Optimization and Machine Learning*, Addison–Wesley, Reading, MA, 1989, pp. 120–124.

A. D. Belegundu
Associate Editor